IVYSPRING INTERNATIONAL PUBLISHER

Theranostics

2019; 9(4): 1125-1143. doi: 10.7150/thno.29566

Research Paper

Microporous polysaccharide multilayer coated BCP composite scaffolds with immobilised calcitriol promote osteoporotic bone regeneration both in vitro and in vivo

Qian Tang[1,2,3], Zhichao Hu[1,2], Haiming Jin[1,2], Gang Zheng[1,2], XingFang Yu[1,2], Gang Wu[4], Haixiao Liu[1,2], Zhenzhong Zhu[3], Huazi Xu[1,2]✉, Changqing Zhang[3]✉, Liyan Shen[1,2]✉

1. Key Laboratory of Orthopaedics of Zhejiang Province, Department of Orthopaedics, The Second Affiliated Hospital and Yuying Children's Hospital of Wenzhou Medical University, 109, Xueyuanxi road, 325027 Wenzhou, China
2. The second School of Medicine, Wenzhou Medical University, 109, Xueyuanxi road, 325027 Wenzhou, China
3. Department of Orthopaedic Surgery Shanghai Jiao Tong University Affiliated Sixth People's Hospital, 600 Yishan Road, Shanghai, 200233, China.
4. Department of Oral Implantology and Prosthetic Dentistry, Academic Centre for Dentistry Amsterdam (ACTA), Vrije University Amsterdam and University of Amsterdam, Amsterdam, Nord-Holland, the Netherlands

Qian Tang and Zhichao Hu contribute equally to this work

✉ Corresponding authors: Liyan Shen, Tel:+86-577-88002760 Email: shenliyan@wmu.edu.cn; Changqing Zhang, Tel: +86-21-64369181 Email: zhangcq@sjtu.edu.cn; Huazi Xu, Tel: +86-13616632111Email: spinexu@163.com

Received: 2018.08.29; Accepted: 2019.01.14; Published: 2019.01.30

Abstract

Incorporating a biomimetic coating and integrating osteoinductive biomolecules into basic bone substitutes are two common strategies to improve osteogenic capabilities in bone tissue engineering. Currently, the underlying mechanism of osteoporosis (OP)-related deficiency of osteogenesis remains unclear, and few treatments target at OP-related bone regeneration. Herein, we describe a self-assembling polyelectrolyte multilayered (PEM) film coating with local immobilisation of calcitriol (Cal) in biphasic calcium phosphate (BCP) scaffolds to promote osteoporotic bone regeneration by targeting the calcium sensing receptor (CaSR).

Methods: The ovariectomy-induced functional changes in bone marrow mesenchymal stem cells (BMSCs), protective effects of Cal, and the potential mechanism were all verified. A PEM film composed of hyaluronic acid (HA) and chitosan (Chi) was prepared through layer-by-layer self-assembly. The morphology, growth behaviour, and drug retention capability of the composite scaffolds were characterised, and their biocompatibility and therapeutic efficacy for bone regeneration were systematically explored *in vitro* and *in vivo*.

Results: The osteogenic differentiation, adhesion, and proliferation abilities of ovariectomised rat BMSCs (OVX-rBMSCs) decreased, in accordance with the deficiency of CaSR. Cal effectively activated osteogenesis in these OVX-rBMSCs by binding specifically to the active pocket of the CaSR structure, while the biomimetic PEM coating augmented OVX-rBMSCs proliferation and adhesion due to its porous surface structure. The PEM-coated scaffolds showed advantages in Cal loading and retention, especially at lower drug concentrations. HA/Chi PEM synergised with Cal to improve the proliferation, adhesion, and osteogenesis of OVX-rBMSCs and promote bone regeneration and BCP degradation in the critical-size calvarial bone defect model of OVX rats.

Conclusion: A composite scaffold based on BCP, created by simply combining a biomimetic PEM coating and Cal immobilisation, could be clinically useful and has marked advantages as a targeted, off-the-shelf, cell-free treatment option for osteoporotic bone regeneration.

Key words: osteoporosis, critical-size bone defect, calcitriol, layer-by-layer assembly, polysaccharide

Introduction

Osteoporosis (OP), a systemic skeletal disease, is characterised by bone mass loss and destruction of microarchitecture due to an imbalance between osteoblasts and osteoclasts, leading to bone fragility

and increasing risk of fractures [1, 2]. This disease affects 200 million people worldwide, especially postmenopausal women [3, 4]. Although most osteoporosis research focuses on fracture prevention using a variety of pharmacological agents [5, 6], repair of bone defects following osteoporotic fracture has begun to draw attention. Combinations of artificial bone grafts, anti-catabolic agents, growth factors, and stem cells have been used for osteoporotic bone regeneration [7-9]. However, few therapeutic agents have been specifically designed to target the depressed osteogenic capacity for bone defects in individuals with osteoporosis. Bone repair strategies used in normal rats have been applied to rats with osteoporosis, with unsatisfying results [10]. Durao et al. evaluated bone regeneration in a calvarial critical-sized bone defect (CSD) filled with deproteinised bovine bone mineral (DBBM). A significant decrease of newly formed bone was observed in ovariectomised (OVX) animals compared with animals given a sham operation after both three and six months of healing [11]. Similar results were reported by Mardas et al., who found that ovariectomy causes an 8.2% decrease in newly formed bone in OVX rats compared with healthy animals in a calvarial CSD model [12]. Thus, osteoporosis-induced depression of bone repair was not only limited to long bones, but also occurred in flat bones. In addition, the underlying mechanism that differentiates osteoporotic rats from normal rats in terms of the ability to form new bone is quite important, and substances that enhance bone regeneration in situations that are pertinent to osteoporosis and its mechanism are of great interest.

Calcitriol (Cal), also known as $1,25(OH)_2D_3$, is a drug used in clinical treatment of osteoporosis that enhances intestinal calcium absorption [13]. Meanwhile, it is also a potent transcriptional activator of osteogenesis-related genes encoding type I collagen, alkaline phosphatase (ALP), and osteocalcin (OCN) in osteoblasts [14, 15]. Local administration of Cal efficiently promoted osteogenesis of osteoblasts [16, 17]. Although the mechanism of Cal-induced tissue mineralisation is still debated, several recent studies have demonstrated that it is correlated with activation of the calcium-sensing receptor (CaSR) in osteoblasts or other cells [18-21]. Insufficient bone mineralisation even with adequate levels of extracellular calcium ($[Ca^{2+}]_e$) has been reported, specifically due to lack of 1,25-dihydroxyvitamin D_3 or functional CaSR [22]. The CaSR may directly regulate skeletal development and bone turnover [18, 22-24]. In addition, González-Vázquez et al. demonstrated that CaSR is a key modulator of $[Ca^{2+}]_e$-mediated proliferation, migration, and osteogenic differentiation of rat bone marrow-derived mesenchymal stem cells (rBMSCs) [25]. Together, these reports suggest underlying cross-talk among $[Ca^{2+}]_e$, Cal, and CaSR, which can lead to a potential therapeutic strategy for bone tissue engineering.

Inorganic materials, such as phosphate and silicate materials [7, 26], have been widely applied in bone reconstruction. However, sole application of such materials in large bone defect areas are insufficient [26, 27], especially when combined with underlying disorders such as diabetes mellitus and osteoporosis, which significantly delayed the process of bone healing [10, 28]. Bio-modification and integration of osteoinductive molecules into inorganic materials are emerging as prevalent methods, and appear to offer an ideal solution in such complicated situations. Establishing biomimetic coatings through various techniques could not only add additional biological functions to the materials, but also retain their overall mechanical properties [29-31]. Among these techniques, layer-by-layer (LbL) self-assembly, which is defined as alternating adsorption of oppositely-charged polyelectrolytes onto a substrate, has been widely used to generate polyelectrolyte multilayered (PEM) films on the surfaces of materials to elevate their biocompatibility [31-33]. PEM films composed of polysaccharides, such as chitosan (Chi) and hyaluronic acid (HA), are of great interest for adjusting cellular behaviour by controlling film mechanical properties [34]. Chi, a linear cationic polysaccharide, has attracted considerable interest due to its good hydrophilicity, biocompatibility, non-toxicity, and adsorption properties. It has been widely studied and been used as a material to promote attachment and growth of various types of cells [35-37]. Moreover, HA, an anionic polysaccharide that is also an extracellular and cell-surface-associated glycosaminoglycan, is thought to be a ligand for the CD44 receptor expressed by mesenchymal stem cells (MSCs), correlating with cell adhesion, proliferation, and differentiation [38]. HA/Chi multilayered film has been widely used to augment the bioactivities of scaffolds [39, 40]. Liu et al. reported that surfaces coated with the HA/Chi film exhibit distinct effects on human MSC adhesion, proliferation, and differentiation [41]. Coincidentally, Li et al. noted that HA/Chi coating promoted artificial ligament graft healing in the bone tunnel via enhancement of cell adhesion and proliferation [42]. Therefore, combining the HA/Chi PEM coating technique with Cal may effectively promote bone repair in osteoporotic individuals.

In this study, we first investigated changes in CaSR expression during the osteoporosis process and determined the activation potency of Cal on CaSR

expression and cell functions. Then we loaded Cal into a porous biphasic calcium phosphate (BCP) scaffold, one of the most widely used inorganic materials in clinical practice of bone repair [26], with a PEM coating of HA/Chi to evaluate cell adhesion, proliferation, and osteogenic capability *in vitro*. The bone regeneration capacity of this method was finally verified using a calvarial CSD model in OVX rats.

Materials and Methods

Materials and reagents

Porous BCP scaffolds were purchased from the National Engineering Research Center for Biomaterials of Sichuan University (Chengdu, China), which were fabricated through H_2O_2 foaming, as described in a previous study [43]. The porous BCP ceramic discs (8 mm diameter × 2 mm height) had a ratio of β-TCP to HAP of 80/20 (w/w). They were microporous with open communicating pores with a mean diameter of 200 μm. The mean porosity was 70%. Chi, polyethylenimine (PEI), 1-ethyl-3-[3-dimethylaminopropyl] carbodiimide hydrochloride (EDC), and N-hydroxysulfosuccinimide (sNHS) were purchased from Aladdin (Shanghai, China). HA was a product of Bloomage Freda Biopharm Co., LTD (Shandong, China). Cal (purity > 98%) and NPS-2143 (purity > 98%) were purchased from Sigma-Aldrich (St. Louis, MO, USA). Antibodies against PCNA, cyclin D1, collagen I, c-fos and β-actin were purchased from Abcam (Cambridge, UK), ICAM-1 antibody, M-CSF and RANKL protein were obtained from R&D Systems (Minneapolis, MN, USA). Mouse anti-OCN was acquired from Santa Cruz Biotechnology (Santa Cruz, CA, USA); anti-CaSR and anti-Runx-2, as well as goat anti-rabbit and anti-mouse IgG-HRP, were purchased from Bioworld (Dublin, OH, USA) and antibodies against CD29, CD34, CD44, CD45, and CD90 were purchased from BioLegend (San Diego, CA, USA). NFATc1 antibodies were from Cell Signaling Technology (Danvers, MA). Secondary antibodies of Alexa Fluor 488-labelled and Alexa Fluor 594-labelled goat anti-rabbit and goat anti-mouse rabbit IgG (H+L) were purchased from Jackson ImmunoResearch (West Grove, PA, USA). 4',6-Diamidino-2-phenylindole (DAPI) was purchased from Beyotime (Shanghai, China). In addition, all cell culturing reagents such as culture medium and 2.5% trypsin were purchased from Gibco (Grand Island, NY, USA).

Establishment of a rat osteoporosis model

Adult female Sprague-Dawley rats (220–250 g, n = 68) were provided by the Animal Center of the Chinese Academy of Science (Shanghai, China). The protocol followed in our study for animal care and use complied with the Guides for the Care and Use of Laboratory Animals of the National Institutes of Health and was approved by the Animal Care and Use Committee of Wenzhou University (wydw2014-0129). The entire *in vivo* experimental procedure is summarised in **Figure S1**. All rats were housed under controlled environment conditions. To induce the osteoporosis model, animals were anaesthetised through intraperitoneal injection of 2% (w/v) pentobarbital (40 mg/kg) following a bilateral ovariectomy according to a previously described method [44]. In brief, 61 rats received bilateral 10-mm linear incisions through the lumbar skin followed by gentle removal of both ovaries. The tissue layers were then repositioned and sutured. As a control, surgery consisting of a skin incision without ovary removal was performed as a sham treatment (seven rats). Carprofen (2 mg/kg) was injected intraperitoneally post-surgery for analgesia. Three months after surgery, three rats from each group were randomly selected for validation of the successful establishment of an osteoporotic model through imageological and histological examination (**Figure S2**). After successful determination of the OVX model, 10 OVX rats and 4 sham-surgery rats were used for isolation of BMSCs, while the remaining 48 OVX rats were further used to establish the calvarial defect model.

In vitro protocol for determination of CaSR expression and Cal effects

BMSCs were isolated from the femurs of OVX and sham-surgery rats and cultured as previously described [45]. The cells were divided into sham and OVX groups with two replicates of each to investigate the functional differences between these two groups. Then, to determine the efficacy of Cal treatment on BMSCs with OVX-induced inhibition of osteogenesis, we randomly divided cells into three groups, control group, Cal (1 nM) treatment group, and Cal plus 0.1 μM NPS-2143 (classical CaSR antagonist) treatment group. To induce osteogenic differentiation of BMSCs, osteogenesis-inducing medium was used, which contained 100 μg/mL ascorbic acid (Sigma), 2 mM β-glycerophosphate (Sigma), and 10 nM dexamethasone (Sigma). The medium was changed every 3 days. Subsequently, western blotting, ALP staining and quantification, immunofluorescence, and molecular docking analyses were performed (see supplemental methods).

PEM film fabrication and crosslinking on BCP scaffolds

The fabrication layer-by-layer self-assembled PEM film was according to previous study [46]. For PEM film deposited on scaffold, BCP discs were first

immersed in PEI solution (5 mg/mL in ddH_2O) for 30 min to adsorb a cationic layer onto the substrate. Then, the discs were rinsed with water to remove loosely bound polyelectrolyte molecules. Thereafter, the discs were alternately immersed in HA solution (3 mg/mL, pH 3.0) and Chi solution (1 mg/mL, pH 4.0) for 10 min, with each layer followed by an intermediate rinse in H_2O with the same pH as the adsorbing solution, until 10.5 bilayers were achieved. For crosslinking, the film-coated BCP discs were incubated in freshly prepared mixed solution of 1-ethyl-3-[3-dimethylaminopropyl] carbodiimide hydrochloride (EDC, 100 mg/mL) and N-hydroxysulfosuccinimide (sNHS, 11 mg/mL) at 4°C overnight. The next day, the discs were thoroughly rinsed in ddH_2O to remove residual EDC and sNHS, and then finally dried in a vacuum oven at 37°C for 4 h. The morphologies of BCP and HA/Chi-BCP were observed by scanning electron microscopy (SEM; see supplemental methods).

Cal loading procedure

For Cal loading, the bare BCP scaffolds and film-coated scaffolds were incubated in solutions of Cal in alcohol at various concentrations (10^{-4}, 10^{-3}, and 10^{-2} M) at 4°C overnight. Then, they were washed with ddH_2O three times to remove any weakly bound or unbound drug and were dried in a vacuum oven at 4°C overnight. To measure the amount of Cal loaded, the scaffolds were dissolved in a mixture of hydrochloric acid/alcohol (v:v = 1:1), and the Cal concentrations in the resulting solutions were tested using a Waters Acquity Ultra Performance Liquid Chromatography (UPLC) instrument with a BEH-C18 (2.1 mm × 50 mm × 1.7 μm) column.

LbL follow-up with QCM-D

Quartz crystal microbalance with dissipation (QCM-D) (E1, Biolin Scientific, Linthicum Heights, MD) was used to monitor the assembly process of HA/Chi films. A gold-coated crystal (QSX 301 quartz crystals, Q-sense) was used for this process. The crystal was cleaned with 2% (V/V) HELLMANEX II (Hellma GmbH, KG, Germany) aqueous solution at 70°C for 15 min before the experiment, followed by thorough rinsing with water and drying under a stream of nitrogen. The crystal was first exposed to PEI solution to render it positively charged. Then, it was successively exposed to HA and Chi solutions to construct the HA/Chi multilayered film on the crystal in an LbL manner. The frequency shifts, ΔF, and dissipations, ΔD, of the fundamental, third, fifth, seventh, ninth, eleventh, and thirteenth harmonics were collected using Qsoft401 software (Biolin Scientific, Linthicum Heights, MD) during the film deposition process. Film thickness was calculated based on these data using Q-Tool software (Biolin Scientific, Linthicum Heights, MD) with a viscoelastic model, assuming the density of the film to be 1100 g/L.

Examination of ion release and drug retention capability

Due to the liposolubility of Cal, which is difficult to detect in phosphate-buffered saline (PBS; data not shown), we determined the remaining mass of Cal in the scaffolds as an indirect measure of the release potency of Cal. Briefly, various doses (10^{-4}, 10^{-3}, and 10^{-2} M) of Cal were loaded onto scaffolds (BCP+Cal and HA/Chi-BCP+Cal, with five scaffolds for each time interval) then weighed and soaked in 1 mL of PBS solution. At the designated time points (1, 2, 5, 8, 12, 18, 25, and 35 days), the scaffolds were collected and dissolved in a mixture of hydrochloric acid and alcohol (v:v = 1:1). The Cal concentration in the resulting solution was tested using a Waters Acquity UPLC instrument with a BEH-C18 (2.1 mm × 50 mm × 1.7 μm) column.

To examine the cumulative amount of calcium ions released, scaffolds from different groups (BCP, BCP+Cal, HA/Chi-BCP, and HA/Chi-BCP+Cal, n = 5 for each) were soaked in 10 mL of simulated body fluid (SBF) [47]. At the chosen time points (1, 2, 5, 8, 12, 18, 25, and 35 days), 1 mL of the supernatant was collected for examination, followed by replacement with 1 mL SBF. The calcium concentration of supernatant at each time point was detected using inductively coupled plasma mass spectroscopy (ICP-MS; Agilent 7500ce series, Agilent Technologies, Sydney, Australia).

Seeding cells in scaffolds

Experiments were performed using four groups: BCP alone (BCP), BCP with Cal (BCP+Cal), film-coated BCP (HA/Chi-BCP), and film-coated BCP with Cal (HA/Chi-BCP+Cal). Before seeding cells, all scaffolds were cleaned in ethanol and then PBS for 15 min each, followed by sterilisation steps with ultraviolet light and ethylene oxide for 15 min each. After drying, 5×10^4 rBMSCs were seeded onto each scaffold. Meanwhile, to examine their osteogenesis capacity, osteogenesis-inducing medium was used. The gene and protein levels of PCNA, cyclin D1, ICAM-1, CaSR, RUNX-2, collagen I, and OCN expression were determined through qRT-PCR (see supplemental methods) and western blot analysis 5 μm thick respectively. Cell viability and morphology on different scaffolds were detected using a Cell Counting Kit-8 (CCK-8; Dojindo Co, Kumamoto,

Japan) and SEM, respectively (see supplemental methods).

Examination of alkaline phosphatase (ALP) activity and collagen synthesis in scaffolds

Quantitative analysis of the ALP level and ALP staining of cells in scaffolds was conducted using methods similar to those used for cells seeded onto plates (see supplemental methods). To examine collagen synthesis in cells seeded onto a scaffold, samples with cells were fixed at day 14 using 4% paraformaldehyde and then rinsed three times in PBS. Then, they were stained with Sirius red (Sigma, USA), washed with 0.1 M acetic acid, and images were captured through a stereomicroscope (Leica, Germany). For quantitative analysis, the stains were subsequently dissolved with 1 mL of destaining solution (0.2 M NaOH:methanol, 1:1) and measured quantitatively at an optical density of 540 nm.

Rat critical-size calvarial defect models

Forty-eight OVX rats further received calvarial surgery for the CSD model. Briefly, after anaesthetisation, an incision was made along the median of the calvarium, and the skin and periosteum were incised to expose the calvarial bone surface. An 8-mm diameter trephine bur was used to carefully drill a standardised round defect around the sagittal suture. During drilling, the surface was irrigated with 0.9% saline solution to cool the skull, and the underlying dura mater was protected to keep it intact. Subsequently, the defect was covered with the various modified BCP discs (BCP alone, BCP with Cal loaded, film-coated BCP, film-coated BCP with Cal loaded; 12 rats in each group). Finally, the periosteum and dermis were closed using 5-0 silk suture. Carprofen (2 mg/kg) was injected intraperitoneally post-surgery for analgesia.

Micro-computed tomography (micro-CT) analysis

After harvesting of specimens at each time point, the calvarium was removed intact and fixed in 4% freshly prepared formaldehyde for 24 h at 4°C. New bone formation in the calvarium was determined using micro-CT (MicroCT m100, SCANCO Medical, Switzerland). The scanning resolution was 25 µm. Next, the three-dimensional reconstructed images were analysed using software (Ray V4.0-4, Switzerland). A consistent volume of interest (VOI), defined as the region where tissue grew into the implants from the margin to the centre, was used to evaluate the level of bone regeneration [48]. Mimics (Materialise, Belgium) software was used for image processing, including two-dimensional reconstruction and quantitative analysis. Two thresholds were identified: one at 225 HU for the soft tissue-bone limit, and the other at 1504 HU for the bone-ceramic limit. Furthermore, the VOI of each specimen was divided into four concentric cylinders from the margin to the centre to study the distribution of bone regeneration within the scaffold. The ratio of bone volume to total volume available in the scaffold (BV/TV) was calculated for various groups. A higher ratio means that more bone had grown into the scaffolds.

Histological analysis

The specimens harvested at 12 weeks post-implantation were fixed in 4% paraformaldehyde for 24 h at 4°C. For slicing of decalcified bones, the sample was decalcified in 10% EDTA solution at 4°C for 4 weeks. Next, the samples were dehydrated using an alcohol gradient, cleared, and embedded in paraffin blocks. Serial lateral sections (5 µm thickness) of each calvarium were obtained and five slides per sample (at 50 µm intervals) were stained with hematoxylin and eosin (H&E) or Masson's trichrome according to the manufacturers' instructions. The stained sections were photographed digitally under a microscope. For undecalcified sections, after embedding in resin, specimens were sawn vertically to the sagittal suture into six slices of 600-µm thickness located 1 mm apart. Slices of each sample were fixed on Plexiglas and carefully polished. The surfaces of the slices were then stained with McNeal's tetrachrome, basic fuchsine, and toluidine blue O. Images were recorded using a stereomicroscope at a final magnification of 10× and saved in colour for histomorphometric analysis of various parameters. Semi-quantitative analysis was carried out using Image-Pro Plus software, version 6.0 (Media Cybernetics, Rockville, MD, USA) to show the relative amounts of bone formation and BCP residue. The area of newly formed mineralised tissue and the remaining BCP volume in each section were calculated and shown as a percentage of total tissue area**.** The protocols for immunohistochemical staining of CaSR, OCN, PCNA, and ICAM-1 are described in the supplemental methods.

Statistical analysis

All experiments were performed independently at least six times. All results are expressed as the mean ± standard deviation (S.D.). Statistical evaluation of the differences among two or more groups was performed via one-way analysis of variance (ANOVA) followed by Tukey's test for comparisons of the control and treatment groups using SPSS statistical software 20.0. Values of $P < 0.05$ were considered indicative of statistical significance.

Results and discussion

Osteoporosis animal model

Osteoporosis has a negative influence on the osseous healing process, which is not only limited to long bones, but also affects the calvarium [10, 49, 50]. Ovariectomy of female animals has been strongly recommended by The Food and Drug Administration (FDA) as the preferred model to imitate osteoporosis in humans [51]. Successful establishment of osteoporosis was verified through X-ray, micro-CT and H&E staining (**Figure S3**).

Previous research confirmed that CaSR played an important role in extracellular calcium ions ($[Ca^{2+}]_e$)-mediated proliferation and osteogenic differentiation of BMSCs [25]. Also, high levels of $[Ca^{2+}]_e$ or polycationic CaSR agonists (for instance neomycin or gadolinium) have been reported to enhance osteoblast proliferation, differentiation, and matrix mineralisation [52, 53]. In addition, the works of Yamauchi et al. and González-Vázquez et al. revealed that overexpression of CaSR stimulated the upregulation of osteogenic markers in MC3T3-E1 cell lines and rBMSCs [25, 54]. By contrast, Chatopadhyay et al. showed that inactivation of CaSR decreased rat calvarial osteoblast proliferation and differentiation [55]. Mechanistically, the activation of CaSR directly stimulated RUNX-2 expression, which is referred to as the master switch of osteogenic differentiation due to its targeting of the transcription of osteoblast-related genes such as those encoding osteocalcin (OCN), type I collagen, and ALP [56-58]. Among these factors, OCN and type I collagen are the main constituents of bone extracellular matrix (ECM) and ALP is responsible for mineralisation of the ECM [58].

In the current study, we examined the expression level of CaSR and changes in the adhesion, proliferation, and osteogenic ability of OVX-rBMSCs. After cultivation in osteogenic-inducing medium for 14 days, western blot analysis showed that the expression levels of Runx-2, collagen I, and OCN (osteogenesis markers) [58] decreased, as did ALP activity, in OVX-rBMSCs compared to those in the sham-surgery group (**Figure 1A–D**). Meanwhile, ovariectomy also inhibited expression of PCNA and cyclin D1 (proliferation markers) [59] as well as ICAM-1 (adhesion marker) [60] in rBMSCs (**Figure 1A–B**). Together, these data demonstrated that osteogenic differentiation, adhesion, and proliferation capacity of rBMSCs all decreased significantly after ovariectomy. Moreover, alteration of the CaSR expression level was consistent with the downregulation in OVX-rBMSCs noted above, and CaSR-positive cells decreased in both the bone marrow and calvarial suture (**Figure 1E–F**). This result suggested that there might be a correlation between deficient CaSR expression and ovariectomy-induced decreases in adhesion, proliferation, and osteogenic differentiation capacity. This change might not be localised solely in long bones, but may also cause problems in flat bones.

Cal treatment

Cal is an agent used for clinical treatment of osteoporosis via promotion of calcium absorption in the intestine, which also targets the osteogenic differentiation of MSCs; however, the specific mechanism remains unclear. Interestingly, previous studies showed that Cal could significantly increase CaSR expression in several organs [19-21]. Here, we studied its effects on OVX-rBMSCs.

To explore whether ovariectomy-induced declines of proliferation, adhesion, and osteogenic differentiation in rBMSCs would be reversed by Cal administration (10^{-9} M) and whether this treatment was associated with CaSR activation, we examined the levels of CaSR, PCNA, cyclin D1, and ICAM-1 as well as the ALP activities in OVX-rBMSCs administered Cal treatment. Western blotting analysis and ALP activity measurement showed that expression levels of CaSR and of osteogenic markers including collagen I, Runx-2, OCN, and ALP, were significantly upregulated in the Cal group and thereafter inhibited by NPS-2143, an allosteric antagonist of CaSR (**Figure 2A–D**). Moreover, using double-labelled immunofluorescence staining of CaSR and Runx-2, we found that Runx-2 expression varied in accordance with changes in CaSR expression (**Figure 2E**). However, the expression levels of PCNA, cyclin D1, and ICAM-1 did not change in the Cal treatment with or without antagonist addition (**Figure 2A–B**). Furthermore, we performed docking analysis of Cal to the tryptophan derivative binding site (an agonist pocket) in the CaSR protein structure; this active pocket is a functional site that is synergised by bivalent cations (such as Ca^{2+} and Mg^{2+}) to co-activate the function of CaSR [61]. Accordingly, the results revealed a high affinity of –8.3 kcal/mol of Cal with the CaSR structure, and the space-filling model illustrated that Cal was completely embedded in the active pocket of CaSR. Meanwhile, the view showing local interactions of protein residues with Cal showed that an important hydrogen bond was formed between Cal and the ASN-102 residue of CaSR. Moreover, the 2D view showed that several hydrophobic bonds existed between Cal and Asp216, Asp275, Gly146, Trp70, Ser147, Gly148, Val149, Tyr218, Thr145, Pro274, Ser272, Ala298, Arg66, Ser302, Ala168, Pro39, and Phe42 (**Figure 2F**). These data suggested that Cal effectively activated osteogenesis

in OVX-rBMSCs, and this phenomenon might be related to its regulation of CaSR. On one hand, Cal not only directly binds to the active pocket of CaSR to upregulate its expression level, but may also synergise with extracellular calcium ions to further improve its function. On the other hand, the increased osteogenic effect of Cal could be abolished after addition of its classic antagonist.

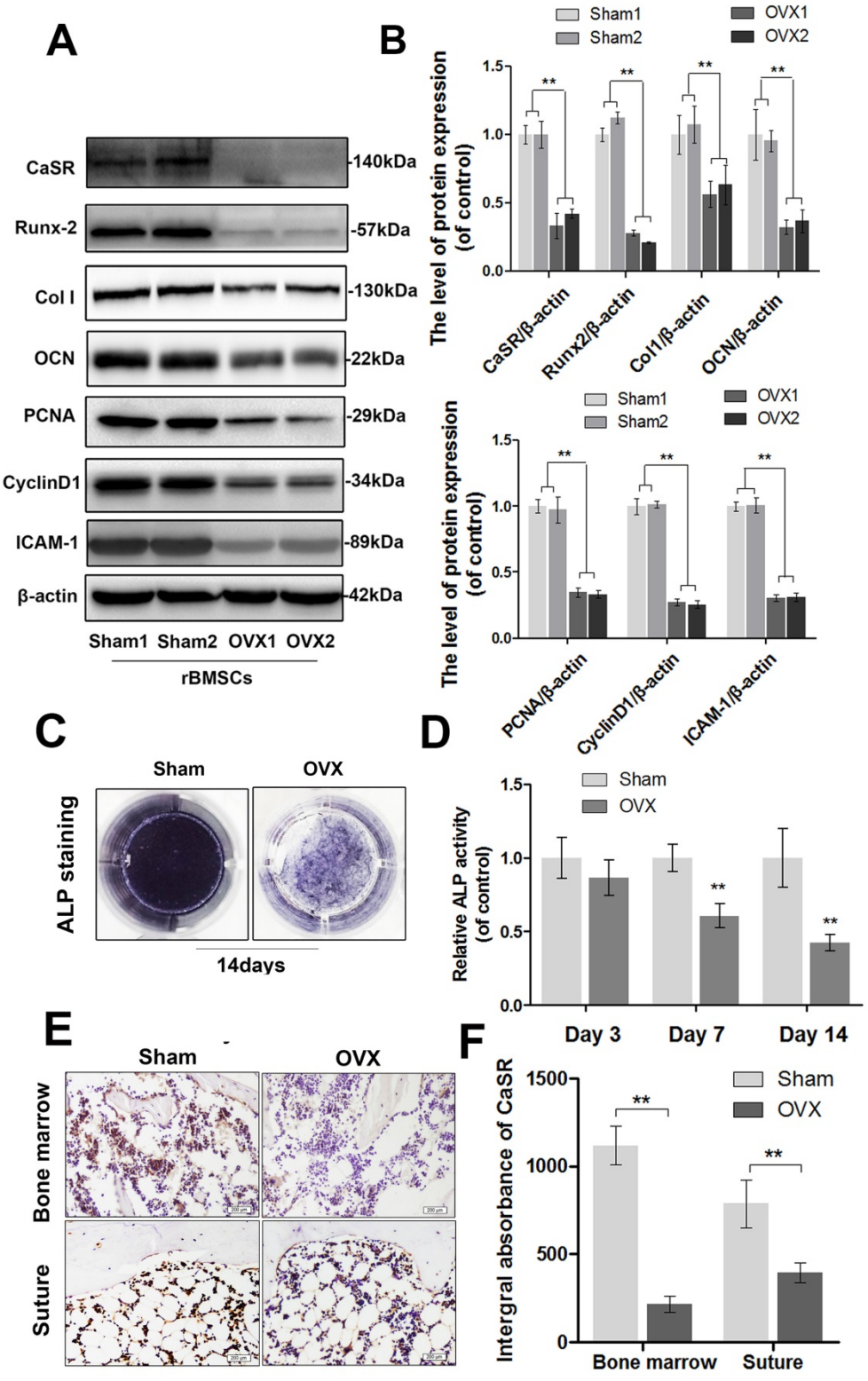

Figure 1. Expression of CaSR and the osteogenic differentiation, proliferation, and adhesion capabilities of sham-rBMSCs and OVX-rBMSCs. (A) Representative western blot results of CaSR, Runx-2, collagen I, OCN, PCNA, cyclin D1, and ICAM-1 expression. **(B)** Quantification of western blot data shown in A. **(C)** Representative images of ALP staining of sham-rBMSCs and OVX-rBMSCs at day 14. **(D)** Quantitative analysis of ALP expression at days 3, 7, and 14. **(E)** Immunohistochemical staining of CaSR expression in the bone marrow and calvarial suture (original magnification 100×, scale bar: 200 μm). **(F)** Quantitative analysis of E. Data are presented as the mean ± S.D. Significant differences between the sham and OVX groups are indicated as ** $P < 0.01$, * $P < 0.05$, $n = 5$.

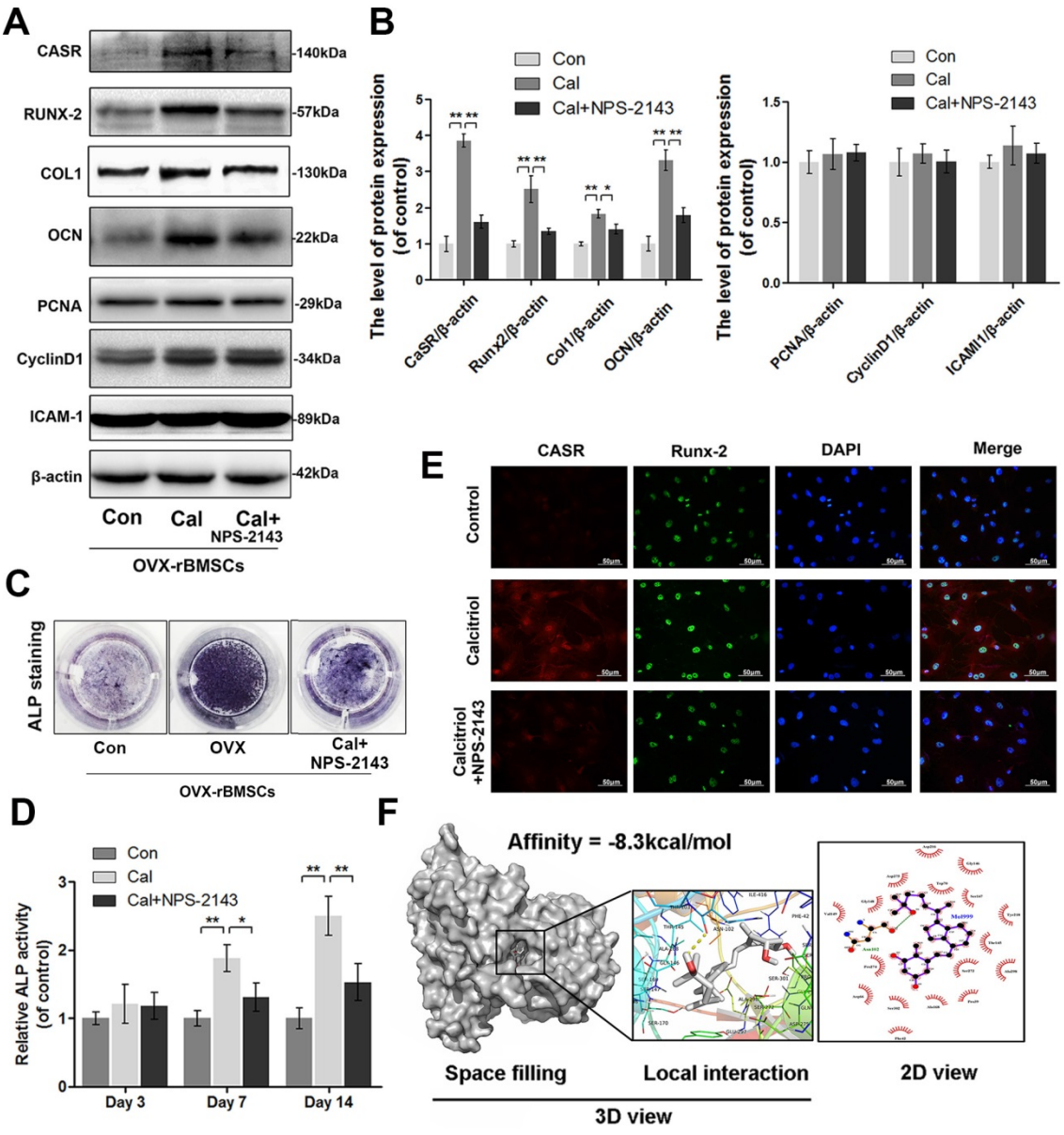

Figure 2. Expression of CaSR and the osteogenic differentiation, proliferation, and adhesion capabilities of OVX-rBMSCs after Cal administration. (A) Representative western blot results for CaSR, Runx-2, collagen I, OCN, PCNA, cyclin D1, and ICAM-1 expression. **(B)** Quantification of western blot data shown in A. **(C)** Representative image of ALP staining of OVX-rBMSCs with Cal and Cal+NPS-2143 treatments at day 14. **(D)** Quantitative analysis of ALP expression at days 3, 7, and 14. **(E)** Immunofluorescence staining of CaSR proteins (red), Runx-2 proteins (green), and DAPI-labelled nucleus (blue). Scale bars are 50 μm. **(F)** Cal docked with the CaSR structure. Docking studies were performed as described in the materials and methods section. A space-filling model showed the binding of Cal in the active binding pocket. The protein residues and hydrogen bonds are shown to have local interactions. Hydrogen bonds and hydrophobic bonds are shown in the 2D view. Data are presented as the mean ± S.D. Significant differences between the treatment and control groups are indicated as ** $P < 0.01$, * $P < 0.05$, $n = 5$.

Although some previous research has reported that CaSR was strongly associated with the proliferation and adhesion capabilities of BMSCs [52, 53], in this study the ovariectomy-induced decreases in proliferation and adhesion in rBMSCs were not reversed with Cal treatment, and thus, these factors might not be associated with the change in CaSR expression. These results indicated that pathways other than CaSR must be involved in ovariectomy-induced inhibition of proliferation and adhesion of rBMSCs, which we recommend exploring in future works.

PEM-coated and Cal-loaded porous BCP scaffolds

As Cal exhibited no enhancing effect on ovariectomy-induced depression of cell proliferation and adhesion, a different strategy was needed to improve OVX-rBMSCs adhesion and proliferation on substrates. Surface modification of substrates is essential for BMSCs differentiation, adhesive interaction, and matrix mineralisation [62]. Previous studies determined that both Chi and HA have good biocompatibility, which benefitted cell proliferation, adhesion, and differentiation [35-40].

To reverse the depression of CaSR expression, adhesion, and proliferation of OVX-rBMSCs, and to promote bone regeneration in OVX rats, we incorporated Cal and an HA/Chi multilayer coating into porous BCP scaffolds. The fabrication procedure is depicted in **Figure 3A**. Briefly, the multilayer film was constructed in an LbL fashion through alternate absorption of HA at pH 3.0 and Chi at pH 4.0, followed by intermediate rinsing steps. After chemical crosslinking, Cal was loaded through a simple post-diffusion method.

QCM-D was employed to monitor the LbL assembly of HA/Chi multilayers onto flat substrates, and the frequency shifts (ΔF) and dissipation differences (ΔD) produced at the harmonic of n = 3 were plotted against layers deposited (**Figure 3B**). Overall, the frequency shifts decreased and dissipation increased steadily as the deposition step increased. Notably, there was a decrease in dissipation and a slightly increase in frequency shift upon the assembly of an HA layer, suggesting that film densification and water extrusion may occur when HA molecules are deposited onto Chi-covered films. Film thickness was estimated using Qsoft, as illustrated in **Figure 3C**, and film thickness increased linearly as the layer pair number increased.

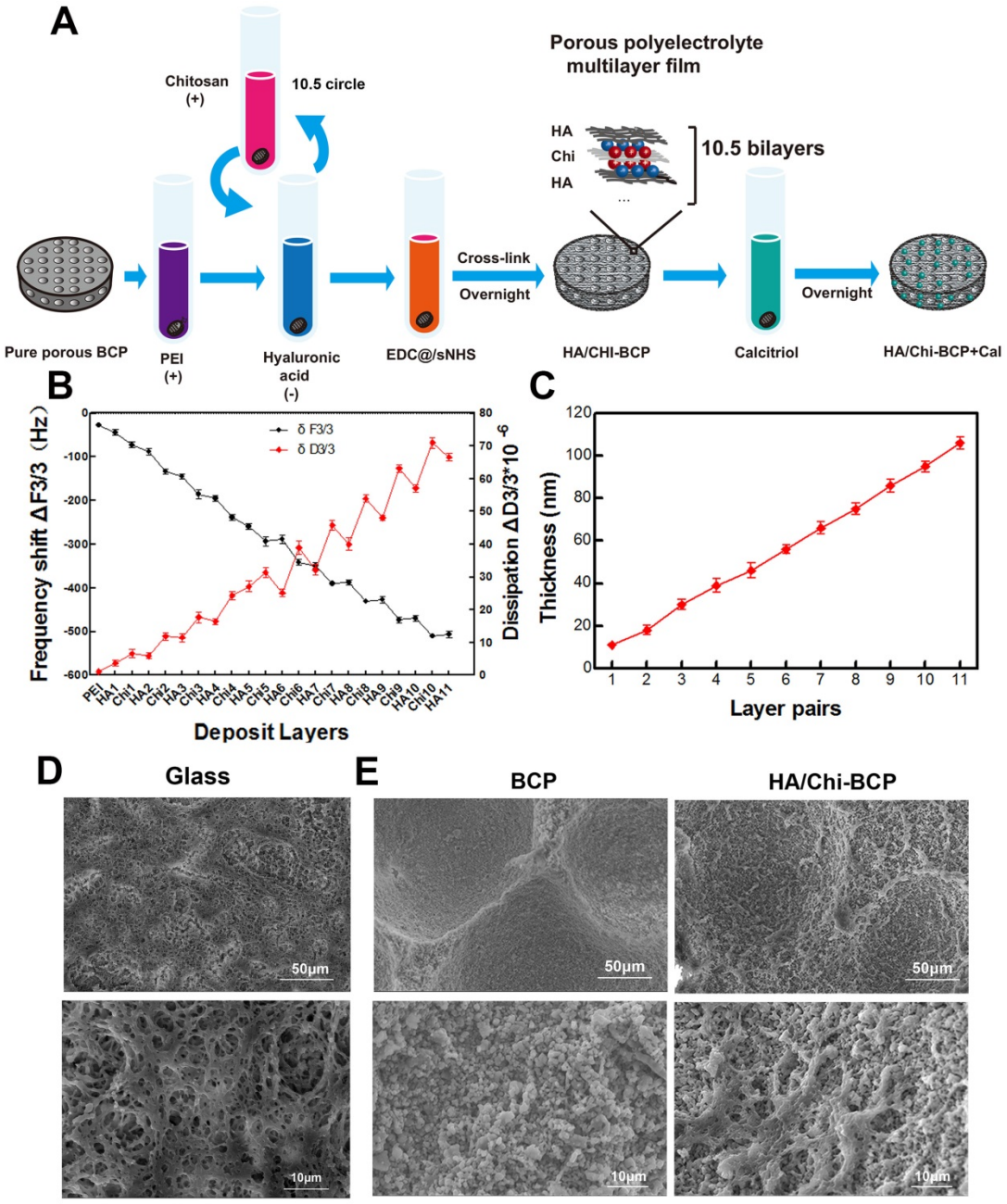

Figure 3. Characters of PEM coating. (A) Schematic illustration of the preparation of a composite porous BCP scaffold coated with an HA/Chi multilayer and loaded with Cal. **(B)** QCM-D data of HA/Chi film build-up, frequency shifts, and dissipations of harmonic n = 3 are shown. **(C)** Film thickness versus layer pairs calculated by Qsoft. **(D)** SEM image of an HA/Chi film built on a glass slide (scale bars: 50 μm, 10 μm). **(E)** SEM image of BCP and HA/Chi-BCP (scale bars: 50 μm, 10 μm).

The surface morphology of films built on glass slides was observed by SEM (**Figure 3D**), and we found that the films had a porous structure with numerous interconnected micropores. These pores may be formed due to the decrease in pH during HA deposition steps [63]. The surface morphology of the porous scaffolds after HA/Chi multilayer coating was also visualised using SEM. As shown in **Figure 3E**, the SEM images revealed high roughness of the bare scaffolds and sub-micrometre scale gaps between particles. For PEM-coated scaffolds, the images showed that the surface BCP was covered with a thin porous film, which had a similar structure as those formed on glass slides. The micropore structure and high porosity of the film made the surface even rougher than that of a bare scaffold.

The drug loading and retention capacities of the substitute are quite essential, especially when used for bone regeneration, which may require several months. We soaked scaffolds with and without PEM coating in Cal solutions of various concentrations for drug loading. The total amount of Cal loaded and the mass retained after washing in PBS were determined through UPLC, and these data are shown in **Figure 4A** and **B**. These results clearly demonstrated that the drug loading amount is highly dependent on the Cal concentration, decreasing almost linearly with the decrease in concentration. When the drug was loaded at a higher concentration (10^{-2} M), there was no significant difference between the two scaffolds in terms of Cal absorption (**Figure 4A**). However, when the drug loading concentration was decreased to 10^{-3} or 10^{-4} M, the porous PEM film-coated BCP scaffold held a greater loading amount compared to the bare BCP scaffold (**Figure 4A**), indicating that a PEM coating may have a drug enrichment capability at low concentrations. Unsurprisingly, due to the extremely low solubility of Cal in water, all scaffolds loaded with various concentrations of Cal exhibited long-term drug retention capability. At every time point, the PEM scaffold carried more drugs than the bare scaffold at low concentration (**Figure 4B**). This pattern suggests that the Cal is a novel agent and is suitable for direct interaction with local cells. In addition, the data suggested that the porous PEM coating provided an advantage in terms of Cal loading and retention when the drug was loaded at relatively low concentrations. Occasionally, the effective concentration of Cal used for *in vitro* administration was as low as 10^{-9} M [64] and higher pharmacological levels of Cal have been reported to inhibit mineral deposition and decrease cell proliferation in a strain-dependent manner in chicken MSCs [65]. Thus, to assure both satisfactory release time and a relatively safe drug concentration, the BCP scaffold immersed in 10^{-3} M Cal solution was adopted for further experiments.

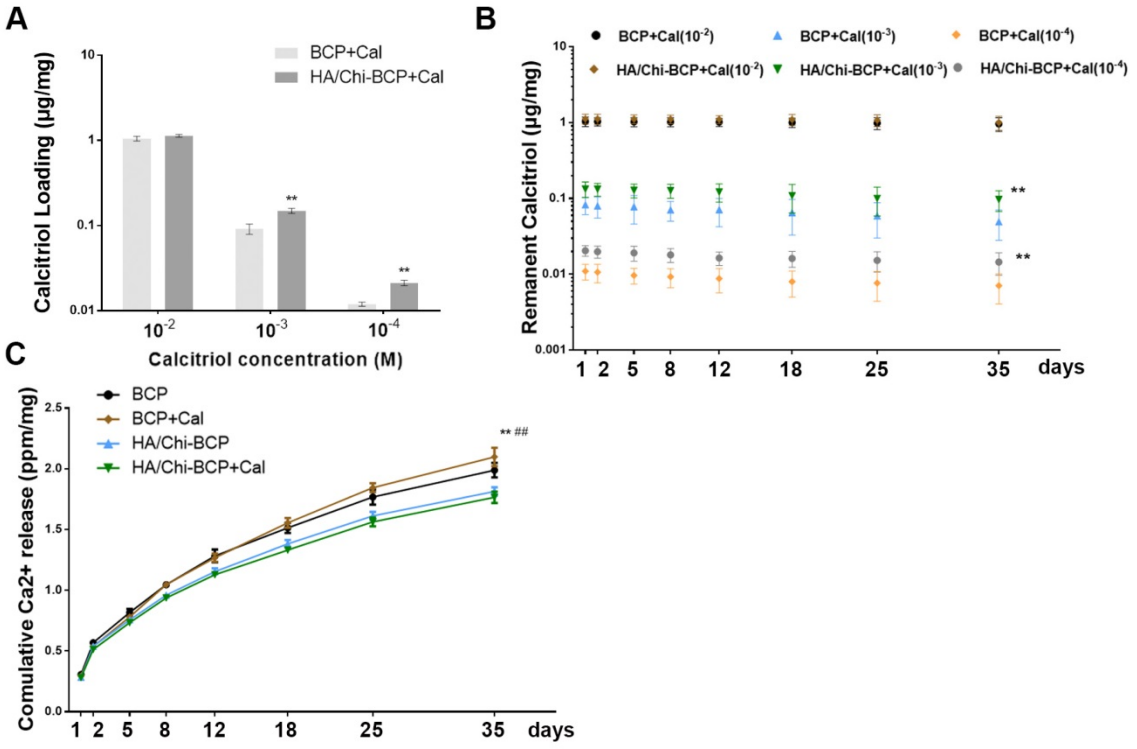

Figure 4. Drug loading and retention ability and ions releasing profile. (A) Cal loading amounts in BCP and HA/Chi-BCP were quantified through UPLC. **(B)** UPLC results of the retained amounts of Cal in BCP and HA/Chi-BCP loaded with drug concentrations of 10^{-2}, 10^{-3}, and 10^{-4} M at 1, 2, 5, 8, 12, 18, 25, and 35 days. **(C)** ICP-MS results of the cumulative release of calcium ions from various scaffolds. Data are presented as the mean ± S.D. Significant differences between the HA/Chi-BCP and bare BCP are indicated as ** $P < 0.01$; differences between the HA/Chi-BCP+Cal and BCP+Cal groups are indicated as ## $P < 0.01$; all n = 5.

Ca^{2+} ions are essential components in bone renewal and regeneration. In our study, the influence of a PEM coating on ion release was tested by incubating scaffolds in SBF. After examination using ICP-MS, the resultant Ca^{2+} concentrations were obtained by subtracting the amount of Ca^{2+} in SBF (100 mg/L). As shown in **Figure 4C**, the concentrations of Ca^{2+} accumulated in SBF after 35 days were 406.10 ± 12.27 and 367.75 ± 7.00 mg/mL for BCP and PEM film-coated BCP, respectively, suggesting a slight reduction in calcium ion release in the porous PEM film-coated BCP scaffold. Furthermore, the loading of Cal did not affect ion release profiles.

Cytocompatibility and functions of scaffolds *in vitro*

To examine the effects of the PEM coating and local immobilisation of Cal on OVX-rBMSCs, we directly seeded the cells into the scaffolds. Their adhesion, proliferation, and osteogenic differentiation properties were tested by means of CCK-8, western blot, and immunostaining assays.

Figure 5A is a schematic illustration of the interface between scaffolds and OVX-rBMSCs, where the PEM coating may promote bone formation by inducing cell adhesion and proliferation, thanks to the film's biocompatible properties including a porous, well cross-linked structure and polysaccharide-derived components. Firstly, the CCK-8 assay was used to quantify cell numbers 3, 7, and 14 days after seeding of OVX-rBMSCs onto the scaffolds (**Figure 5B**). Compared with the control group, the seeding rates of each scaffold were over 50%, indicating that these scaffolds had good biocompatibility. Although the increase in cell number on porous PEM coating did not reach a statistically significant difference after 3 days of cultivation, the differences were enhanced when the culturing time was increased to 7 days and further amplified after 14 days. Meanwhile, the CCK-8 assay data revealed that the addition of Cal did not have much impact on cell viability. Cell morphology on the scaffolds was observed using SEM on day 14. As shown in **Figure 5C**, more cells were found on the porous PEM film-coated scaffolds than on uncoated scaffolds. The magnified image clearly showed that cells on the HA/Chi film-coated and Cal-loaded scaffolds were more plump and extensive, and they even grew beneath the film. To further verify whether the HA/Chi multilayer coating enhanced OVX-rBMSCs adhesion and proliferation, the protein expression levels of PCNA, cyclin D1, and ICAM-1 were determined using western blot analysis at day 14 (**Figure 5D–E**). The results showed that expression levels of all three proteins increased if cells were seeded on porous PEM film-coated scaffolds, which was consistent with the CCK-8 assay data. Together, these results indicated that the porous PEM coating favoured cell proliferation and adhesion.

Figure 6A illustrates the possible mechanism for Cal, which is immobilised in the BCP scaffold and interacts with OVX-rBMSCs, subsequently promoting their osteogenic differentiation. Specific targeting of CaSR and consequent acceleration of its bonding with Ca2+ might be the underlying molecular mechanism. Osteogenic differentiation was first evaluated through determination of osteogenesis-related gene expression after 7, 14, and 21 days of growth in induced differentiation medium on different scaffolds. The expression levels of all osteogenesis-related genes were greatly enhanced when Cal was incorporated (**Figure S4**). Relative protein expression was examined using western blot analysis. As shown in **Figure 6B–C**, the expression levels of CaSR, collagen I, Runx-2, and OCN in OVX-rBMSCs 14 days after seeding onto scaffolds increased significantly in the presence of Cal. The HA/Chi multilayer coating also caused limited enhancement of osteogenesis-related protein expression, while the combination of the multilayer coating and Cal showed the strongest activation of osteogenic differentiation of OVX-rBMSCs. ALP activity and collagen secretion assays were also carried out at day 14 to verify the osteogenic differentiation of OVX-rBMSCs on different scaffolds. As shown in **Figure 6D–E**, both the HA/Chi film and Cal had positive effects on ALP expression, and therefore the combination of the two greatly enhanced ALP expression up to 2-fold above that of the bare BCP. Similar results were obtained using Sirius Red staining (**Figure 6F–G**), where denser collagen deposition was found on the HA/Chi-BCP+Cal scaffold.

In vivo bone formation

To identify osteogenesis on BCP scaffolds with HA/Chi coating and/or Cal, an 8-mm calvarial CSD was created in osteoporotic rats, which is a significant indicator of future clinical translational application. At 6 and 12 weeks post-transplantation, calvaria were extracted and analysed through imageological examination and histological analysis.

Three-dimensional micro-CT reconstruction images revealed the morphology of the newly formed bone. The overall morphologies are shown in **Figure 7A**, and magnified images in the coronal and axial views are presented in **Figure 7B**. Although new bone had formed and infiltrated the bone cavity in all four groups of rats implanted with different scaffolds after both 6 and 12 weeks of healing, more new bone formation occurred with the modified BCP scaffolds, especially when Cal was incorporated.

Quantitative analysis (**Figure 7C**) of the newly formed bone volume demonstrated that a limited amount of new bone was formed in the BCP scaffold group (14.34 ± 2.03% and 20.07 ± 3.20% at 6 and 12 weeks, respectively). More newly formed bone was observed in the HA/Chi-BCP group (28.34 ± 3.56% and 35.93 ± 6.20% for 6 and 12 weeks, respectively), indicating that the HA/Chi coating was also effective *in vivo*. Significant acceleration of bone regeneration was achieved (40.81 ± 3.91% and 48.63 ± 4.08% at 6 and 12 weeks, respectively) in the Cal-BCP group, confirming the osteogenic efficacy of Cal. Due to the conjugation of both Cal and HA/Chi multilayers on the BCP scaffolds, the amount of newly-regenerated bone tissue increased further in the HA/Chi-BCP+Cal group (50.33 ± 4.67% and 63.38 ± 6.76% at 6 and 12 weeks, respectively). Compared to bare BCP scaffolds, more new bone was formed during the time between 6 and 12 weeks with Cal-BCP scaffolds (40.81 ± 3.91% to 48.63 ± 4.08% versus 14.34 ± 2.03% to 20.07 ± 3.20%), indicating that Cal may still be released from the BCP after 6 weeks.

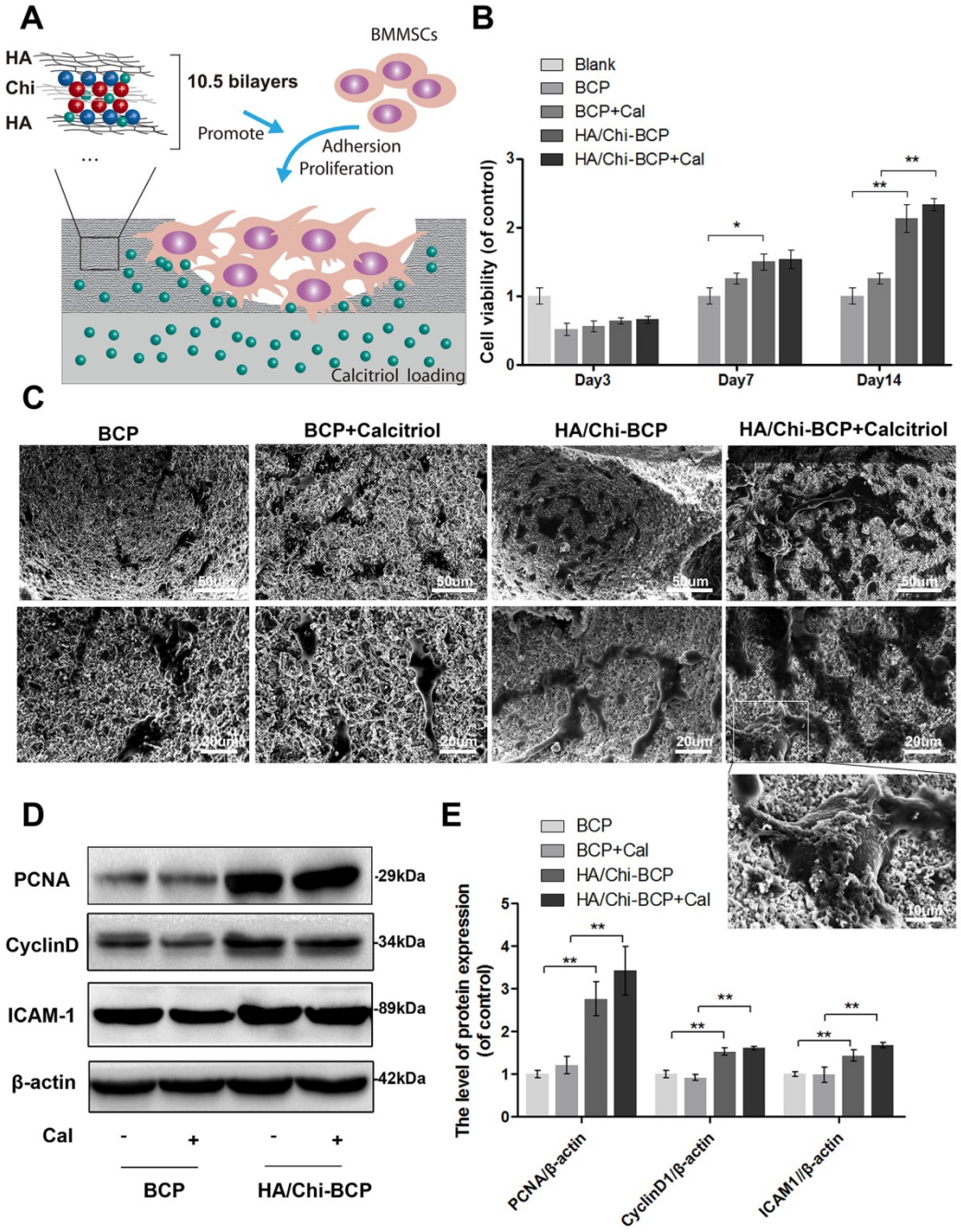

Figure 5. Effects of different scaffolds on OVX-rBMSCs proliferation and adhesion. (A) Schematic illustration of the effects of porous HA/Chi film on cell proliferation and adhesion. **(B)** Cell viability on various scaffolds tested using the CCK-8 assay. **(C)** SEM images of the morphology of OVX-rBMSCs on different scaffolds at day 14 (scale bars: 50, 20, and 10 μm). **(D–E)** Representative western blot results and quantification data for PCNA, cyclin D1, and ICAM-1. Data are presented as the mean ± S.D. Significant differences among scaffold groups are indicated as ** P < 0.01, * P < 0.05, n = 5.

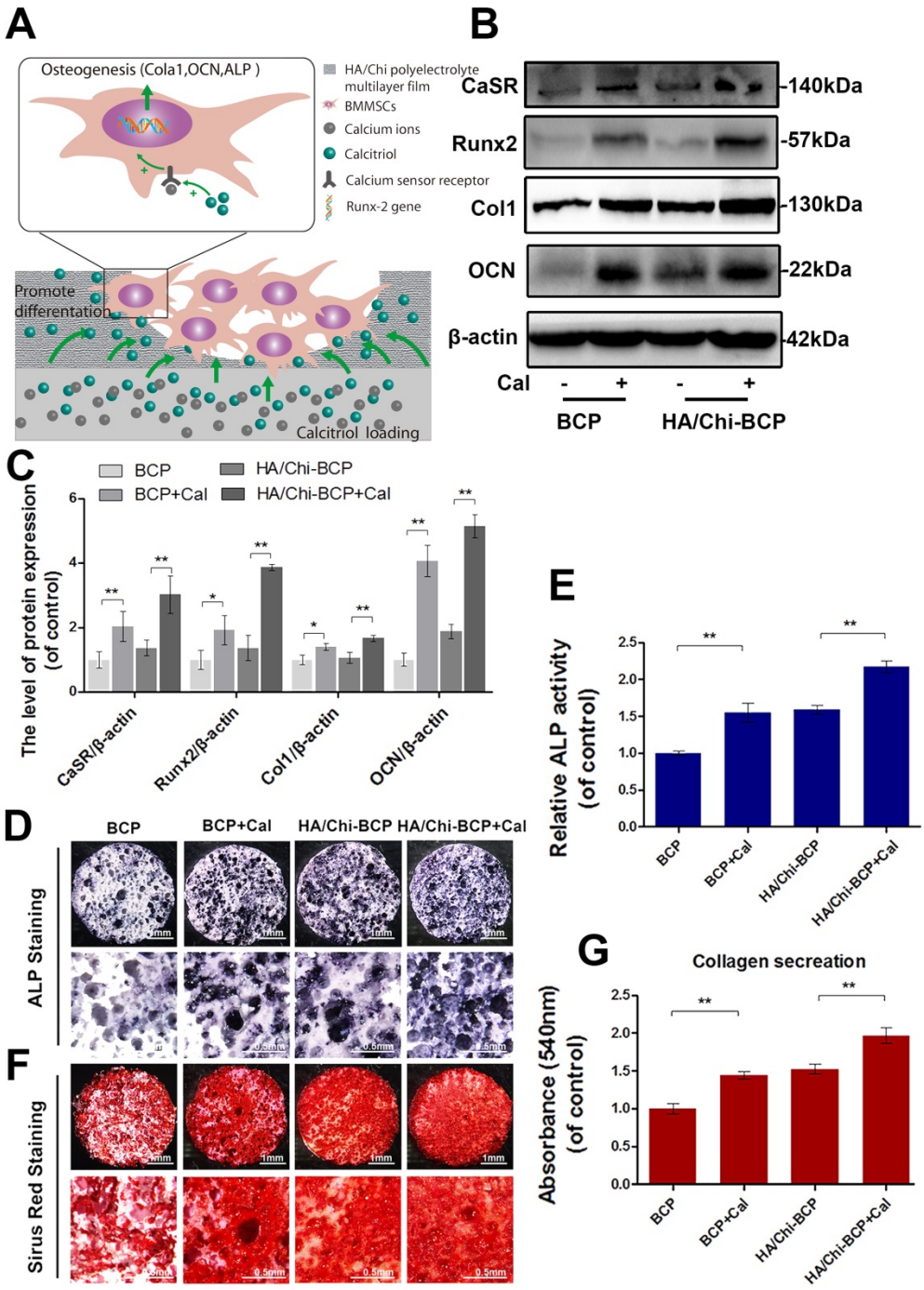

Figure 6. Effects of different scaffolds on OVX-rBMSCs osteogenic differentiation. (A) Schematic illustration of the effects of Cal loaded in BCP scaffolds on osteogenic differentiation of cells. **(B–C)** Representative western blot results and quantification of CaSR, Runx-2, Col I, and OCN expression. **(D)** Representative images of ALP staining results for rBMSCs after cultivation on scaffolds for 14 days. Original magnifications 7.5×, 30×; Scale bars: 1 mm, 0.5 mm. **(E)** Quantitative colourimetric results of ALP activities of cells on different BCP scaffolds. **(F)** Representative images of Sirius red staining results for rBMSCs after cultivation on scaffolds for 14 days. Original magnification 7.5×, 30×; Scale bars: 1 mm, 0.5 mm. **(G)** Quantitative results of collagen secretion by cells on various BCP scaffolds. Data are presented as the mean ± S.D. Significant differences among scaffold groups are indicated as ** $P < 0.01$, * $P < 0.05$, $n = 5$.

A remarkable increase was observed with HA/Chi-BCP+Cal scaffolds (50.33 ± 4.67% to 63.38 ± 6.76%) during the second 6 weeks of healing. This result can be ascribed to the advantages of the HA/Chi film, which elevates both scaffold cytocompatibility and Cal retention. To further investigate the process of bone ingrowth into the scaffolds, the entire VOI (volume of interest) was classified into four layers according to distance from the sample boundary (**Figure 7D**), and the BV/TV values of each layer were measured and calculated (**Figure 7E**). More nascent bone was formed in the layer closest to the boundary, and the amount of new bone decreased from the boundary to the centre of the scaffold. Again, a synergetic effect of HA/Chi film and Cal on osteogenic regeneration was observed.

Unlike the bare BCP group, where new bone preferred to grow on the boundary of the defects, nascent bone tissue formed simultaneously both on the boundary and in the centre of the defects when HA/Chi films, Cal, or both were incorporated. Subsequently, more bone was formed in all four layers of the scaffolds for the HA/Chi-BCP+Cal group. These phenomena might be explained by two results: 1) The biocompatibility of the scaffold was greatly improved by HA/Chi multilayer coating, and thus more cells survived on the scaffold including in the central part, and 2) the osteogenic differentiation of OVX-rBMSCs or other cells was reversed and activated by local interaction with Cal. Therefore, the HA/Chi multilayer coating combined with Cal can improve bone regeneration under osteoporotic conditions using classical BCP scaffolds.

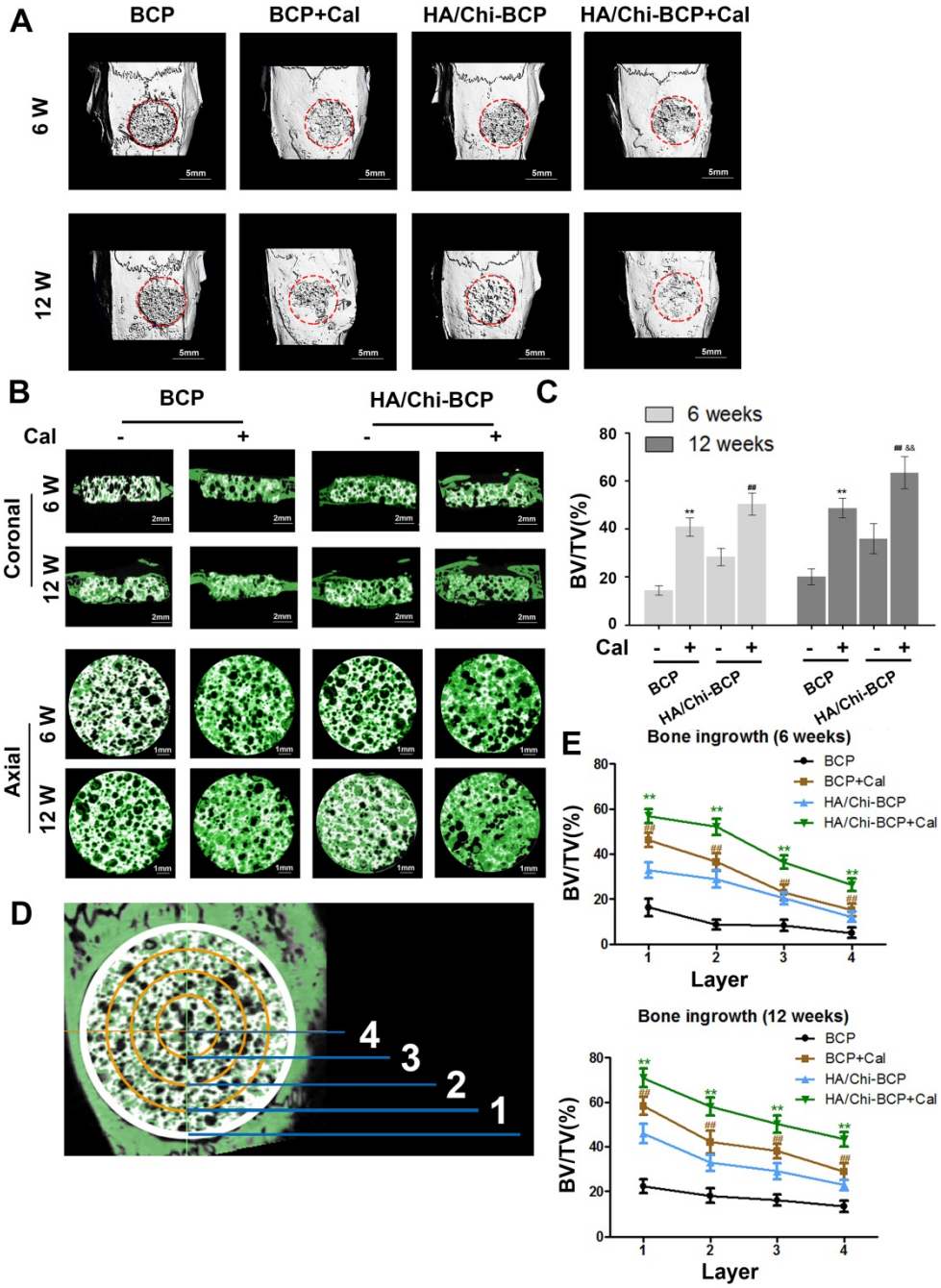

Figure 7. Micro-CT analysis of the effects of various BCP scaffolds on new bone formation in the critical-size bone defect model of OVX rats. (A) Three-dimensional reconstruction of micro-CT images of the various scaffolds implanted in the rat calvarium at 6 and 12 weeks (scale bars: 5 mm). **(B)** Two-dimensional reconstruction of micro-CT images of various scaffolds implanted in the rat calvarium at 6 and 12 weeks (the white colour component shows the remaining scaffold, bone that grew around and into the scaffolds is labelled in green) (scale bars: 2 mm for coronal images and 1 mm for axial images). **(C)** Regenerated bone volumes on the various scaffolds were quantified as bone volume divided by total volume (BV/TV). **(D)** General sketch of the scaffold, which was divided into four layers. **(E)** Percentages of bone volume regenerated into the scaffold in different layers from the edge to the centre. Data are presented as the mean ± S.D. Significant differences among scaffold groups are indicated as ** P < 0.01, * P < 0.05, compared with BCP; ## P < 0.01, # P < 0.05 compared with HA/Chi-BCP, and && P < 0.01, & P < 0.05 compared with BCP+Cal; for each group, n = 5.

To further confirm new bone tissue formation results obtained from micro-CT analysis and to analyse the new bone morphology in a more detailed way, we performed histology assays on both decalcified and undecalcified samples. For each specimen, decalcified transverse sections of the entire calvarium were initially evaluated at low magnification to identify the regions of interest. Both H&E staining (**Figure S5**) and Masson's trichrome staining (**Figure 8A**) revealed that samples from the bare BCP group typically exhibited little bone formation within the defect regions at 12 weeks post-implantation, whereas greater mineralised areas were observed from the BCP+Cal groups. Although several collagen fibres and immature bone were found in the defects of the HA/Chi-BCP groups, few mineralised tissues were observed. Moreover, compared to the other three groups, far more mature bone formation was detected in the HA/Chi-BCP+Cal group at 12 weeks. In addition, high-magnification views of both the margin and central areas of defects supported the conclusion that the HA/Chi-BCP+Cal group obtained the greatest benefit in terms of bone ingrowth.

To further quantify bone volume and remaining BCP volume without the disturbance caused by decalcification, we stained the undecalcified section with McNeal's tetrachrome, basic fuchsine, and toluidine blue O (**Figure 8B**). Here, new bone tissue appeared pink, and blue colour represented the remaining BCP scaffolds. As shown in **Figure 8B**, larger amounts and significantly greater distributions of new bone formation were found in the HA/Chi-BCP+Cal group compared to the other three groups. Meanwhile, the HA/Chi-BCP+Cal group showed more pronounced degradation of BCP scaffolds than others. Histomorphometric results were consistent with histologic findings (**Figure 8C**), providing additional evidence of the contribution of the microporous HA/Chi multilayer and Cal to bone restoration under osteoporotic conditions.

The major drawback of BCP scaffolds in clinical trials was their slow degradation, which needed to be accelerated. BCP served as a scaffold and a source of calcium and phosphate ions for the formation of new bone. The more actively the bone regenerated, the more BCP was degraded. In this way, the histology assay of the undecalcified section showed that HA/Chi-BCP+Cal scaffolds could promote BCP degradation.

Additionally, to demonstrate the specific molecular mechanisms of different scaffolds *in vivo*, we performed immunohistochemical staining of CaSR, OCN, PCNA, and ICAM-1 proteins. Representative images and quantitative analysis results are shown in **Figure 8D–E**. CaSR- and OCN-positive areas were elevated in the BCP+Cal group compared to the bare BCP group, but there was no significant difference in PCNA or ICAM-1 expression between these two groups. These results suggested that the contribution of Cal to osteogenesis in bone defects might be related to the regulation of CaSR expression. Moreover, although the HA/Chi-BCP group showed little positive effect on osteogenesis according to the limited level of OCN expression, it showed higher PCNA and ICAM-1 expression levels, indicating that microporous films on the scaffold surface markedly promoted cell proliferation and adhesion. Certainly, the HA/Chi-BCP+Cal group showed incremental effects in osteogenesis, cell proliferation, and adhesion with higher expression levels of CaSR, OCN, PCNA, and ICAM-1 compared to the other three groups.

Local administration of bioactive compounds can lead to facile and economical therapies for tissue engineering. In this study, we started with a mechanistic investigation, demonstrating for the first time the role of CaSR in osteoporosis-induced depression of osteogenesis in BMSCs. Additionally, Cal was revealed to be a novel agent that efficiently targets CaSR and acts synergistically with extracellular calcium ions to reverse this condition. We designed the composite BCP scaffold to improve both drug loading capacity and biocompatibility. On one hand, the results showed that these scaffolds are a good candidate for Cal loading and that Cal loaded into them was capable of interacting directly with local cells, such as BMSCs, to promote osteogenic differentiation *in vitro* (**Figure 2, 6**) and subsequent bone regeneration *in vivo* (**Figure 7, 8**), under osteoporotic conditions. However, aside from improving osteogenesis, the effects of composite scaffolds to osteoclastogenesis were also explored. Although the effects of either calcitriol or CaSR on osteoclasts activities are controversial in previous publications [23, 66-68], in this study, our results showed that the calcitriol loaded scaffolds could increase the expression of CaSR but decrease the c-fos and NFATc1 expression (the marker of osteoclastogenesis) of bone marrow monocytes (BMMs), under the stimulation of 50ng/mL of RANKL (Figure S6. A-B). Meanwhile, the number of TRAP positive cells were decreased in calcitriol loaded scaffolds both in vitro and in vivo section of tissue. (Figure S6. C-D). It indicated that the calcitriol loaded scaffold could also inhibit osteoclastogenesis, and the potential mechanism behind it might be associated with the activation of CaSR. Moreover, scaffold degradation might also be associated with significant bone ingrowth and accelerated calcium

absorption and utilisation after CaSR activation, but this point requires further study. Meanwhile, the PEM film coating added to the retention of Cal, and Cal appeared to be immobilised on the scaffold (**Figure 4B**). However, how this immobilised Cal is internalised by cells, such as the OVX-rBMSCs used in this study, and how immobilised Cal and the free Cal (added directly to the culture medium, reached the cells via releasing from scaffold, etc.) differ in their cellular interactions and bone regeneration activities, are also topics for future studies.

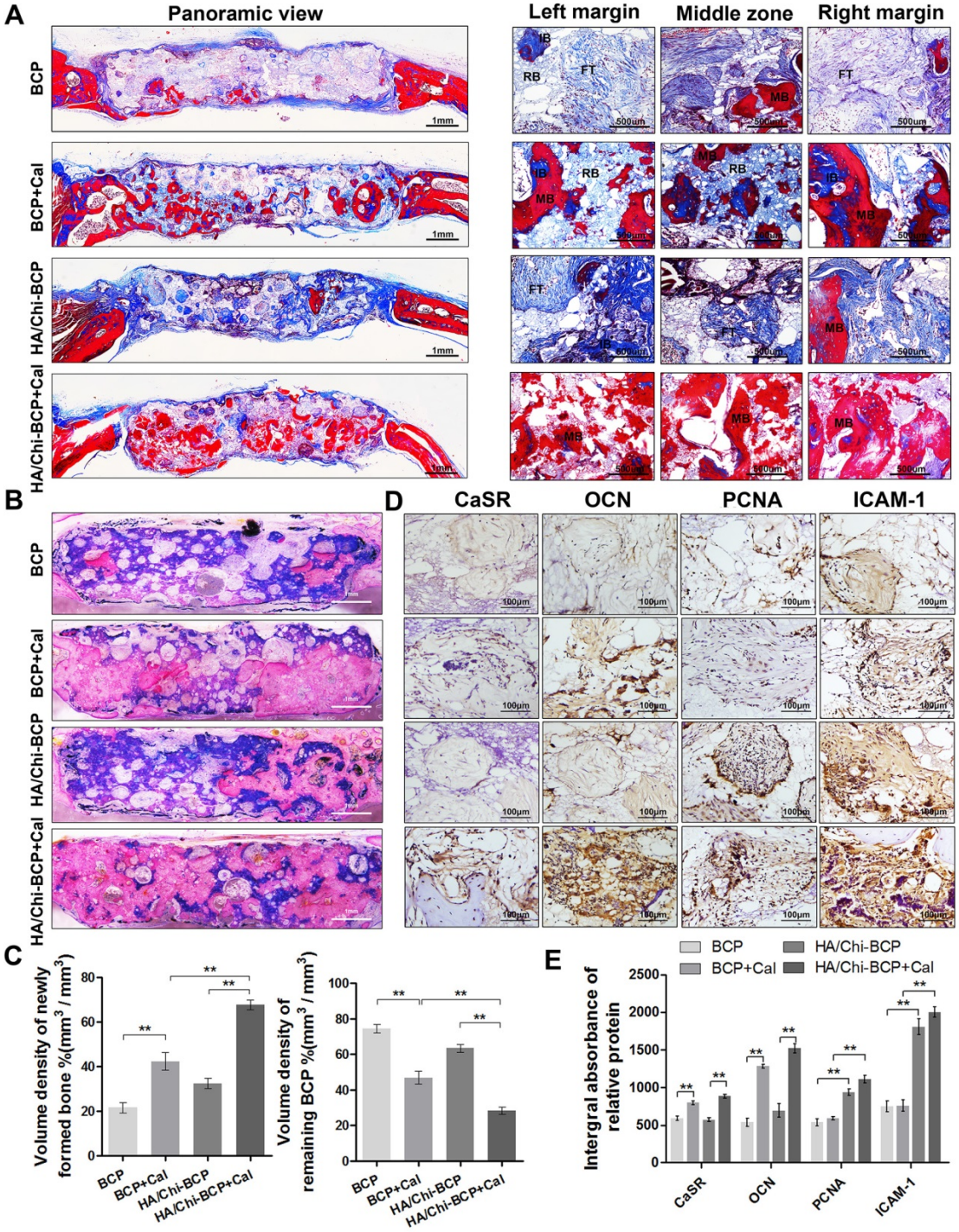

Figure 8. Histological evaluation of new bone formation in the critical-size bone defect model of OVX rats after 12 weeks. (A) Masson's trichrome staining of decalcified bone including full-image and magnified views from different sites in the defect area. FT, fibrous tissue; IB, immature bone; MB, mature bone; and RB, resident BCP. Scale bars, 1 mm, 500 μm; magnification 50×, 200×. **(B)** Representative full image of undecalcified bone; the section was stained with McNeal's tetrachrome, basic fuchsine, and toluidine blue O. Pink staining represents bone tissue and blue staining represents remaining BCP (original magnification 10×; scale bar, 1 mm). **(C)** Histomorphometric measurements of the volume density of total newly formed bone (pink) and remaining BCP scaffold (blue) at 12 weeks after implantation according to McNeal's staining. Values are shown as the mean ± S.D. ** $P < 0.01$, * $P < 0.05$, indicating significant differences between groups. **(D)** Representative images showing immunohistochemical staining of CaSR, OCN, PCNA, and ICAM-1 expression in the defect area (original magnification, 100×; scale bar, 100 μm). **(E)** Quantification data for CaSR, OCN, PCNA, and ICAM-1 expression based on D. Data are presented as the mean ± S.D. Significant differences among groups are indicated as ** $P < 0.01$, * $P < 0.05$, n = 5.

On the other hand, incorporation of the HA/Chi coating augmented cell viability on the scaffold. Although polysaccharide-derived PEM film has long been considered biocompatible, cell behaviour on films is dependent on their physical properties. Picart's group studied the effect of film stiffness on cellular adhesion and found that cells remained round on soft native films, while they adhered and spread quickly on stiff and well-crosslinked films [69, 70]. In addition, film surface morphology and, specifically, microscale surface structures have a strong influence on the setting of cells on the films. Rough surfaces or porous surface structures may be more beneficial for cell viability [71, 72]; the research of Cristina et al. showed that a nanopore structure of PEM film significantly supported cell adhesion, proliferation, and migration compared to smooth and nonporous surfaces [73]. In our study, pH-adjusted LbL assembly, which provides an easy method for fabricating rough or porous PEM films [63], was coupled with strong crosslinking, and a porous PEM film with microscale, interconnected pores was constructed (**Figure 3**). These films were beneficial for cell adhesion and proliferation both *in vitro* (**Figure 5**) and *in vivo* (**Figure 7, 8**). Because the depression of bone regeneration caused by osteoporosis occurred not only in long bone but also in flat bone [12] (**Figure 1E–F**), we tested the composite scaffold in a calvarial CSD model in OVX rats as a first trial, and obtained encouraging results. However, the effect of the composite scaffold should be further verified in long bones, as osteoporotic-induced bone failure occurs more often in load-bearing bones such as the humerus, lumbar vertebrae, and hip.

Conclusions

In this work, we reported the environmentally friendly fabrication of a composite scaffold based on classical BCP for bone regeneration under osteoporotic conditions. According to ovariectomy-induced downregulation of osteogenic differentiation, proliferation, and adhesion capabilities, Cal was immobilised into BCP scaffolds as a therapeutic agent to promote OVX-rBMSCs osteogenic capacity, and then pH-tuned microporous HA/Chi multilayer films were coated onto BCP scaffolds to improve the cytocompatibility of the scaffolds for OVX-rBMSCs. *In vitro* experiments revealed that the combination of HA/Chi coating and Cal not only enhanced OVX-rBMSCs adhesion and proliferation, but also greatly enhanced osteogenic differentiation by reversing the depression of CaSR expression caused by OVX. More importantly, a similar trend was observed in bone regeneration among groups of OVX rats in a calvarial CSD model.

Thus, our findings provide instructive insights into the local use of classical anti-osteoporotic drugs with the assistance of multilayer coating, which may have great potential for applications in the fields of bone tissue engineering and regenerative medicine.

Abbreviations

OP: osteoporosis; Cal: calcitriol; PEM: polyelectrolyte multilayered films; HA: hyaluronic acid; Chi: chitosan; BCP: biphasic calcium phosphate; CaSR: Calcium-sensing receptor; QCM-D: Quartz crystal microbalance with dissipation; SEM: scanning electron microscope; OVX: ovariectomy; CSD: critical sized bone defect; ALP: alkaline phosphatase; OCN: osteocalcin; rBMSCs: rat bone marrow-derived mesenchymal stem cells; PEI: polyethylenimine; EDC: 1-Ethyl-3-[3-dimethylaminopropyl] carbodiimide hydrochloride; sNHS: N-hydroxysulfosuccinimide.

Supplementary Material

Supplementary methods and figures.
http://www.thno.org/v09p1125s1.pdf

Acknowledgements

We are highly thankful to Dr. Zhiyan Hu from Key Laboratory of Anesthesiology of Zhejiang Province for assistance with UPLC analysis. Financial support from the National Natural Science Funding of China (41506091, 81501869), Zhejiang provincial Public welfare project (2017C33035), Key Laboratory of Orthopaedics of Zhejiang Province (ZJGK1806Y) and Medical and health science and technology project of Zhejiang Province (2016YKA139) are well acknowledged.

Competing Interests

The authors have declared that no competing interest exists.

References

1. Rachner TD, Khosla S, Hofbauer LC. Osteoporosis: now and the future. Lancet. 2011; 377: 1276-87.
2. Verron E, Gauthier O, Janvier P, Pilet P, Lesoeur J, Bujoli B, et al. In vivo bone augmentation in an osteoporotic environment using bisphosphonate-loaded calcium deficient apatite. Biomaterials. 2010; 31: 7776-84.
3. Cooper C, Campion G, Melton LJ, 3rd. Hip fractures in the elderly: a world-wide projection. Osteoporosis international : a journal established as result of cooperation between the European Foundation for Osteoporosis and the National Osteoporosis Foundation of the USA. 1992; 2: 285-9.
4. Wright NC, Looker AC, Saag KG, Curtis JR, Delzell ES, Randall S, et al. The recent prevalence of osteoporosis and low bone mass in the United States based on bone mineral density at the femoral neck or lumbar spine. Journal of bone and mineral research : the official journal of the American Society for Bone and Mineral Research. 2014; 29: 2520-6.
5. Bonn D. New ways with old bones. Osteoporosis researchers look for drugs to replace hormone replacement therapy. Lancet. 2004; 363: 786-7.
6. Deal C. Potential new drug targets for osteoporosis. Nature clinical practice Rheumatology. 2009; 5: 20-7.
7. Lin K, Xia L, Li H, Jiang X, Pan H, Xu Y, et al. Enhanced osteoporotic bone regeneration by strontium-substituted calcium silicate bioactive ceramics. Biomaterials. 2013; 34: 10028-42.

8. Zhang Y, Cheng N, Miron R, Shi B, Cheng X. Delivery of PDGF-B and BMP-7 by mesoporous bioglass/silk fibrin scaffolds for the repair of osteoporotic defects. Biomaterials. 2012; 33: 6698-708.
9. Li KC, Chang YH, Yeh CL, Hu YC. Healing of osteoporotic bone defects by baculovirus-engineered bone marrow-derived MSCs expressing MicroRNA sponges. Biomaterials. 2016; 74: 155-66.
10. Calciolari E, Mardas N, Dereka X, Kostomitsopoulos N, Petrie A, Donos N. The effect of experimental osteoporosis on bone regeneration: Part 1, histology findings. Clinical oral implants research. 2016.
11. Durao SF, Gomes PS, Colaco BJ, Silva JC, Fonseca HM, Duarte JR, et al. The biomaterial-mediated healing of critical size bone defects in the ovariectomized rat. Osteoporosis international : a journal established as result of cooperation between the European Foundation for Osteoporosis and the National Osteoporosis Foundation of the USA. 2014; 25: 1535-45.
12. Mardas N, Schwarz F, Petrie A, Hakimi AR, Donos N. The effect of SLActive surface in guided bone formation in osteoporotic-like conditions. Clinical oral implants research. 2011; 22: 406-15.
13. Tilyard MW, Spears GF, Thomson J, Dovey S. Treatment of postmenopausal osteoporosis with calcitriol or calcium. The New England journal of medicine. 1992; 326: 357-62.
14. Thompson L, Wang S, Tawfik O, Templeton K, Tancabelic J, Pinson D, et al. Effect of 25-hydroxyvitamin D3 and 1 alpha,25 dihydroxyvitamin D3 on differentiation and apoptosis of human osteosarcoma cell lines. Journal of orthopaedic research : official publication of the Orthopaedic Research Society. 2012; 30: 831-44.
15. Yang D, Turner AG, Wijenayaka AR, Anderson PH, Morris HA, Atkins GJ. 1,25-Dihydroxyvitamin D3 and extracellular calcium promote mineral deposition via NPP1 activity in a mature osteoblast cell line MLO-A5. Molecular and Cellular Endocrinology. 2015; 412: 140-7.
16. Liu H, Cui J, Feng W, Lv S, Du J, Sun J, et al. Local administration of calcitriol positively influences bone remodeling and maturation during restoration of mandibular bone defects in rats. Materials science & engineering C, Materials for biological applications. 2015; 49: 14-24.
17. Yoon SJ, Park KS, Kim MS, Rhee JM, Khang G, Lee HB. Repair of Diaphyseal Bone Defects with Calcitriol-Loaded PLGA Scaffolds and Marrow Stromal Cells. Tissue Engineering. 2007; 13: 1125-33.
18. Yamaguchi T. The calcium-sensing receptor in bone. Journal of bone and mineral metabolism. 2008; 26: 301-11.
19. Brown AJ, Zhong M, Finch J, Ritter C, McCracken R, Morrissey J, et al. Rat calcium-sensing receptor is regulated by vitamin D but not by calcium. The American journal of physiology. 1996; 270: F454-60.
20. Liu G, Hu X, Chakrabarty S. Vitamin D mediates its action in human colon carcinoma cells in a calcium-sensing receptor-dependent manner: downregulates malignant cell behavior and the expression of thymidylate synthase and survivin and promotes cellular sensitivity to 5-FU. International journal of cancer. 2010; 126: 631-9.
21. Mary A, Henaut L, Boudot C, Six I, Brazier M, Massy ZA, et al. Calcitriol prevents in vitro vascular smooth muscle cell mineralization by regulating calcium-sensing receptor expression. Endocrinology. 2015; 156: 1965-74.
22. Rodriguez L, Tu C, Cheng Z, Chen TH, Bikle D, Shoback D, et al. Expression and functional assessment of an alternatively spliced extracellular Ca2+-sensing receptor in growth plate chondrocytes. Endocrinology. 2005; 146: 5294-303.
23. Goltzman D, Hendy GN. The calcium-sensing receptor in bone--mechanistic and therapeutic insights. Nature reviews Endocrinology. 2015; 11: 298-307.
24. Chang W, Tu C, Bajra R, Komuves L, Miller S, Strewler G, et al. Calcium sensing in cultured chondrogenic RCJ3.1C5.18 cells. Endocrinology. 1999; 140: 1911-9.
25. Gonzalez-Vazquez A, Planell JA, Engel E. Extracellular calcium and CaSR drive osteoinduction in mesenchymal stromal cells. Acta biomaterialia. 2014; 10: 2824-33.
26. Bouler JM, Pilet P, Gauthier O, Verron E. Biphasic calcium phosphate ceramics for bone reconstruction: A review of biological response. Acta biomaterialia. 2017; 53: 1-12.
27. Jang J-W, Yun J-H, Lee K-I, Jang J-W, Jung U-W, Kim C-S, et al. Osteoinductive activity of biphasic calcium phosphate with different rhBMP-2 doses in rats. Oral Surgery, Oral Medicine, Oral Pathology and Oral Radiology. 2012; 113: 480-7.
28. Greenhill C. Stem cells: Bone healing in diabetes mellitus. Nature reviews Endocrinology. 2017; 13: 128.
29. Amin Yavari S, Ahmadi SM, van der Stok J, Wauthle R, Riemslag AC, Janssen M, et al. Effects of bio-functionalizing surface treatments on the mechanical behavior of open porous titanium biomaterials. Journal of the mechanical behavior of biomedical materials. 2014; 36: 109-19.
30. Maia FR, Bidarra SJ, Granja PL, Barrias CC. Functionalization of biomaterials with small osteoinductive moieties. Acta biomaterialia. 2013; 9: 8773-89.
31. Crouzier T, Sailhan F, Becquart P, Guillot R, Logeart-Avramoglou D, Picart C. The performance of BMP-2 loaded TCP/HAP porous ceramics with a polyelectrolyte multilayer film coating. Biomaterials. 2011; 32: 7543-54.
32. Decher G. Fuzzy Nanoassemblies: Toward Layered Polymeric Multicomposites. Science. 1997; 277: 1232-7.
33. Boudou T, Crouzier T, Ren K, Blin G, Picart C. Multiple functionalities of polyelectrolyte multilayer films: new biomedical applications. Advanced materials. 2010; 22: 441-67.
34. Richert L, Lavalle P, Payan E, Shu XZ, Prestwich GD, Stoltz JF, et al. Layer by layer buildup of polysaccharide films: physical chemistry and cellular adhesion aspects. Langmuir : the ACS journal of surfaces and colloids. 2004; 20: 448-58.
35. Suh JK, Matthew HW. Application of chitosan-based polysaccharide biomaterials in cartilage tissue engineering: a review. Biomaterials. 2000; 21: 2589-98.
36. Di Martino A, Sittinger M, Risbud MV. Chitosan: a versatile biopolymer for orthopaedic tissue-engineering. Biomaterials. 2005; 26: 5983-90.
37. He J, Wu F, Wang D, Yao R, Wu Y, Wu F. Modulation of cationicity of chitosan for tuning mesenchymal stem cell adhesion, proliferation, and differentiation. Biointerphases. 2015; 10: 04A304.
38. Manferdini C, Guarino V, Zini N, Raucci MG, Ferrari A, Grassi F, et al. Mineralization behavior with mesenchymal stromal cells in a biomimetic hyaluronic acid-based scaffold. Biomaterials. 2010; 31: 3986-96.
39. Tan GK, Dinnes DL, Butler LN, Cooper-White JJ. Interactions between meniscal cells and a self assembled biomimetic surface composed of hyaluronic acid, chitosan and meniscal extracellular matrix molecules. Biomaterials. 2010; 31: 6104-18.
40. Funakoshi T, Majima T, Iwasaki N, Yamane S, Masuko T, Minami A, et al. Novel chitosan-based hyaluronan hybrid polymer fibers as a scaffold in ligament tissue engineering. Journal of biomedical materials research Part A. 2005; 74: 338-46.
41. Liu ZM, Gu Q, Xu ZK, Groth T. Synergistic effect of polyelectrolyte multilayers and osteogenic growth medium on differentiation of human mesenchymal stem cells. Macromolecular bioscience. 2010; 10: 1043-54.
42. Li H, Ge Y, Zhang P, Wu L, Chen S. The effect of layer-by-layer chitosan-hyaluronic acid coating on graft-to-bone healing of a poly(ethylene terephthalate) artificial ligament. Journal of biomaterials science Polymer edition. 2012; 23: 425-38.
43. Li X, Guo B, Xiao Y, Yuan T, Fan Y, Zhang X. Influences of the steam sterilization on the properties of calcium phosphate porous bioceramics. Journal of materials science Materials in medicine. 2016; 27: 5.
44. Thompson DD, Simmons HA, Pirie CM, Ke HZ. FDA Guidelines and animal models for osteoporosis. Bone. 1995; 17: 125S-33S.
45. Zhu H, Guo ZK, Jiang XX, Li H, Wang XY, Yao HY, et al. A protocol for isolation and culture of mesenchymal stem cells from mouse compact bone. Nature protocols. 2010; 5: 550-60.
46. Del Hoyo-Gallego S, Perez-Alvarez L, Gomez-Galvan F, Lizundia E, Kuritka I, Sedlarik V, et al. Construction of antibacterial poly(ethylene terephthalate) films via layer by layer assembly of chitosan and hyaluronic acid. Carbohydrate polymers. 2016; 143: 35-43.
47. Kokubo T, Takadama H. How useful is SBF in predicting in vivo bone bioactivity? Biomaterials. 2006; 27: 2907-15.
48. Oest ME, Dupont KM, Kong HJ, Mooney DJ, Guldberg RE. Quantitative assessment of scaffold and growth factor-mediated repair of critically sized bone defects. Journal of orthopaedic research : official publication of the Orthopaedic Research Society. 2007; 25: 941-50.
49. Durao SF, Gomes PS, Silva-Marques JM, Fonseca HR, Carvalho JF, Duarte JA, et al. Bone regeneration in osteoporotic conditions: healing of subcritical-size calvarial defects in the ovariectomized rat. The International journal of oral & maxillofacial implants. 2012; 27: 1400-8.
50. He YX, Zhang G, Pan XH, Liu Z, Zheng LZ, Chan CW, et al. Impaired bone healing pattern in mice with ovariectomy-induced osteoporosis: A drill-hole defect model. Bone. 2011; 48: 1388-400.
51. Calciolari E, Donos N, Mardas N. Osteoporotic Animal Models of Bone Healing: Advantages and Pitfalls. Journal of investigative surgery : the official journal of the Academy of Surgical Research. 2016: 1-9.
52. Tharmalingam S, Daulat AM, Antflick JE, Ahmed SM, Nemeth EF, Angers S, et al. Calcium-sensing receptor modulates cell adhesion and migration via integrins. The Journal of biological chemistry. 2011; 286: 40922-33.
53. Xiao G, Gopalakrishnan R, Jiang D, Reith E, Benson MD, Franceschi RT. Bone morphogenetic proteins, extracellular matrix, and mitogen-activated protein kinase signaling pathways are required for osteoblast-specific gene expression and differentiation in MC3T3-E1 cells. Journal of bone and mineral research : the official journal of the American Society for Bone and Mineral Research. 2002; 17: 101-10.
54. Yamauchi M, Yamaguchi T, Kaji H, Sugimoto T, Chihara K. Involvement of calcium-sensing receptor in osteoblastic differentiation of mouse MC3T3-E1 cells. American journal of physiology Endocrinology and metabolism. 2005; 288: E608-16.
55. Chattopadhyay N, Yano S, Tfelt-Hansen J, Rooney P, Kanuparthi D, Bandyopadhyay S, et al. Mitogenic action of calcium-sensing receptor on rat calvarial osteoblasts. Endocrinology. 2004; 145: 3451-62.
56. Yasukawa T, Hayashi M, Tanabe N, Tsuda H, Suzuki Y, Kawato T, et al. Involvement of the calcium-sensing receptor in mineral trioxide aggregateinduced osteogenic gene expression in murine MC3T3-E1 cells. Dental materials journal. 2017.
57. Weng JJ, Su Y. Nuclear matrix-targeting of the osteogenic factor Runx2 is essential for its recognition and activation of the alkaline phosphatase gene. Biochimica et biophysica acta. 2013; 1830: 2839-52.
58. Franceschi RT, Xiao G. Regulation of the osteoblast-specific transcription factor, Runx2: responsiveness to multiple signal transduction pathways. Journal of cellular biochemistry. 2003; 88: 446-54.

59. Hu H, Chen M, Dai G, Du G, Wang X, He J, et al. An Inhibitory Role of Osthole in Rat MSCs Osteogenic Differentiation and Proliferation via Wnt/beta-Catenin and Erk1/2-MAPK Pathways. Cellular physiology and biochemistry : international journal of experimental cellular physiology, biochemistry, and pharmacology. 2016; 38: 2375-88.
60. Chang W, Kim R, Park SI, Jung YJ, Ham O, Lee J, et al. Enhanced Healing of Rat Calvarial Bone Defects with Hypoxic Conditioned Medium from Mesenchymal Stem Cells through Increased Endogenous Stem Cell Migration via Regulation of ICAM-1 Targeted-microRNA-221. Molecules and cells. 2015; 38: 643-50.
61. Zhang C, Zhang T, Zou J, Miller CL, Gorkhali R, Yang JY, et al. Structural basis for regulation of human calcium-sensing receptor by magnesium ions and an unexpected tryptophan derivative co-agonist. Science advances. 2016; 2: e1600241.
62. Gribova V, Auzely-Velty R, Picart C. Polyelectrolyte Multilayer Assemblies on Materials Surfaces: From Cell Adhesion to Tissue Engineering. Chemistry of materials : a publication of the American Chemical Society. 2012; 24: 854-69.
63. Fu J, Ji J, Shen L, Kuller A, Rosenhahn A, Shen J, et al. pH-amplified exponential growth multilayers: a facile method to develop hierarchical micro- and nanostructured surfaces. Langmuir : the ACS journal of surfaces and colloids. 2009; 25: 672-5.
64. Hong HH, Hong A, Yen TH, Wang YL. Potential Osteoinductive Effects of Calcitriol on the m-RNA of Mesenchymal Stem Cells Derived from Human Alveolar Periosteum. BioMed research international. 2016; 2016: 3529561.
65. Pande VV, Chousalkar KC, Bhanugopan MS, Quinn JC. Super pharmacological levels of calcitriol (1,25-(OH)2D3) inhibits mineral deposition and decreases cell proliferation in a strain dependent manner in chicken mesenchymal stem cells undergoing osteogenic differentiation in vitro. Poultry science. 2015; 94: 2784-96.
66. Vincent C, Kogawa M, Findlay DM, Atkins GJ. The generation of osteoclasts from RAW 264.7 precursors in defined, serum-free conditions. Journal of bone and mineral metabolism. 2009; 27: 114-9.
67. Li A, Cong Q, Xia X, Leong WF, Yeh J, Miao D, et al. Pharmacologic Calcitriol Inhibits Osteoclast Lineage Commitment via the BMP-Smad1 and IkappaB-NF-kappaB Pathways. Journal of bone and mineral research : the official journal of the American Society for Bone and Mineral Research. 2017; 32: 1406-20.
68. Santa Maria C, Cheng Z, Li A, Wang J, Shoback D, Tu CL, et al. Interplay between CaSR and PTH1R signaling in skeletal development and osteoanabolism. Seminars in cell & developmental biology. 2016; 49: 11-23.
69. Ren K, Crouzier T, Roy C, Picart C. Polyelectrolyte multilayer films of controlled stiffness modulate myoblast cells differentiation. Adv Funct Mater. 2008; 18: 1378-89.
70. Gribova V, Gauthier-Rouviere C, Albiges-Rizo C, Auzely-Velty R, Picart C. Effect of RGD functionalization and stiffness modulation of polyelectrolyte multilayer films on muscle cell differentiation. Acta biomaterialia. 2013; 9: 6468-80.
71. Deligianni DD, Katsala ND, Koutsoukos PG, Missirlis YF. Effect of surface roughness of hydroxyapatite on human bone marrow cell adhesion, proliferation, differentiation and detachment strength. Biomaterials. 2001; 22: 87-96.
72. Khang D, Lu J, Yao C, Haberstroh KM, Webster TJ. The role of nanometer and sub-micron surface features on vascular and bone cell adhesion on titanium. Biomaterials. 2008; 29: 970-83.
73. Hajicharalambous CS, Lichter J, Hix WT, Swierczewska M, Rubner MF, Rajagopalan P. Nano- and sub-micron porous polyelectrolyte multilayer assemblies: biomimetic surfaces for human corneal epithelial cells. Biomaterials. 2009; 30: 4029-36.